communications physics

A Nature Portfolio journal

Article

https://doi.org/10.1038/s42005-026-02547-1

Emergent epithelial elasticity governed by interfacial surface mechanics and substrate interaction

Check for updates

Urška Andrenšek [1,2] ✉ & Matej Krajnc [2]

During the life of animals, epithelial tissues undergo extensive deformations–first to form organs during embryogensis and later to preserve integrity and function in adulthood. To what extent these deformations resemble that of non-living elastic materials is not well understood. We derive an elasticity theory of epithelia, supported by a thin layer of extracellular material and the stroma, in which the mechanics of individual cells are dominated by differential interfacial tensions stemming from cell cortical tension and adhesion. Upon coarse-graining a discrete cell-level mechanics model, we obtain a harmonic deformation energy and derive the critical conditions for the elastic instability, where an initially flat tissue either buckles out of plane or forms wrinkles. Due to the distinct origin of elasticity, the scaling of the critical buckling load and the wrinkling wavelength with layer's thickness is fundamentally different than in solid plates. The theory also naturally describes reversal of the groove-to-crest thickness-modulation phase–a recently observed epithelial shape feature which cannot be explained by the classical elasticity theory. Our work provides a guideline for understanding the relative role of cell surface tensions and the interaction of tissues with substrates during epithelial morphogenesis.

The structure and form of epithelial tissues are intricately connected to their specific functions within an organ. While the mostly protective role of the skin epithelium, for instance, requires smooth and stratified tissue architecture, epithelia of the digestive tract assume single-cell-thick corrugated structures, so as to optimize the exchange of nutrients. These distinct shapes begin to emerge during embryonic development, when the organism undergoes tissue-scale shape changes, transforming initially smooth epithelia into compartmentalized and differentiated cellular structures that eventually develop into fully functional organisms[1–3].

While the detailed shape- and structural changes during epithelial morphogenesis are underlined by comprehensive biochemical patterning with specific spatial and temporal dynamics[4–7], the more general aspects of the shape formation rely on physical mechanisms such as buckling, wrinkling, and folding. Many of these deformation modes can be interpreted in the context of thin-plate elasticity. Whether a plate will buckle out of plane upon uniaxial compression depends on its thickness h. In particular, in the limit of small deformation, the elastic energy of the plate associated with pure compression scales with the thickness as $W_c \propto h$, whereas the elastic energy associated with buckling scales as $W_b \propto h^3$. Consequently, thin plates tend to buckle out of plane under externally applied uniaxial load, whereas thick plates initially compress while remaining flat[8–10]. Eventually, even thick media undergo surface instabilities once the external compression exceeds the Biot threshold[11,12].

This interplay between bending and compression is fundamental to understanding the physical basis of epithelial morphogenesis and the resulting complex tissue architectures. Indeed, the corrugated epithelial patterns such as villi and crypts have been previously explained through a relative growth of the fast-renewing intestinal epithelium against a mostly static stroma[13–16]. The area mismatch at the epithelium-stroma interface, caused by the differential growth, induces elastic stresses, leading to the formation of wrinkles with a characteristic wavelength. The wavelength is determined by a competition between the thin epithelium, which tends to buckle out of plane, and the thick stroma, which prefers pure compression[17–22].

However, the underlying analogy between epithelia and solid plates may disregard some cell-scale specific mechanics and thus may not always be justified. Indeed, as proposed by Thompson[23], the stresses in epithelia may largely be concentrated at cells' surfaces, making them behave more like liquid droplets and less like classic solid plates, where stresses are distributed throughout the volume. While surface tension can be incorporated in the elastic plate theory[21,24], such approach assumes that the tissue itself still behaves like a homogeneous elastic plate and neglects its cellularized

[1]Faculty of Mathematics and Physics, University of Ljubljana, Ljubljana, Slovenia. [2]Jožef Stefan Institute, Ljubljana, Slovenia. ✉e-mail: urska.andrensek@ijs.si

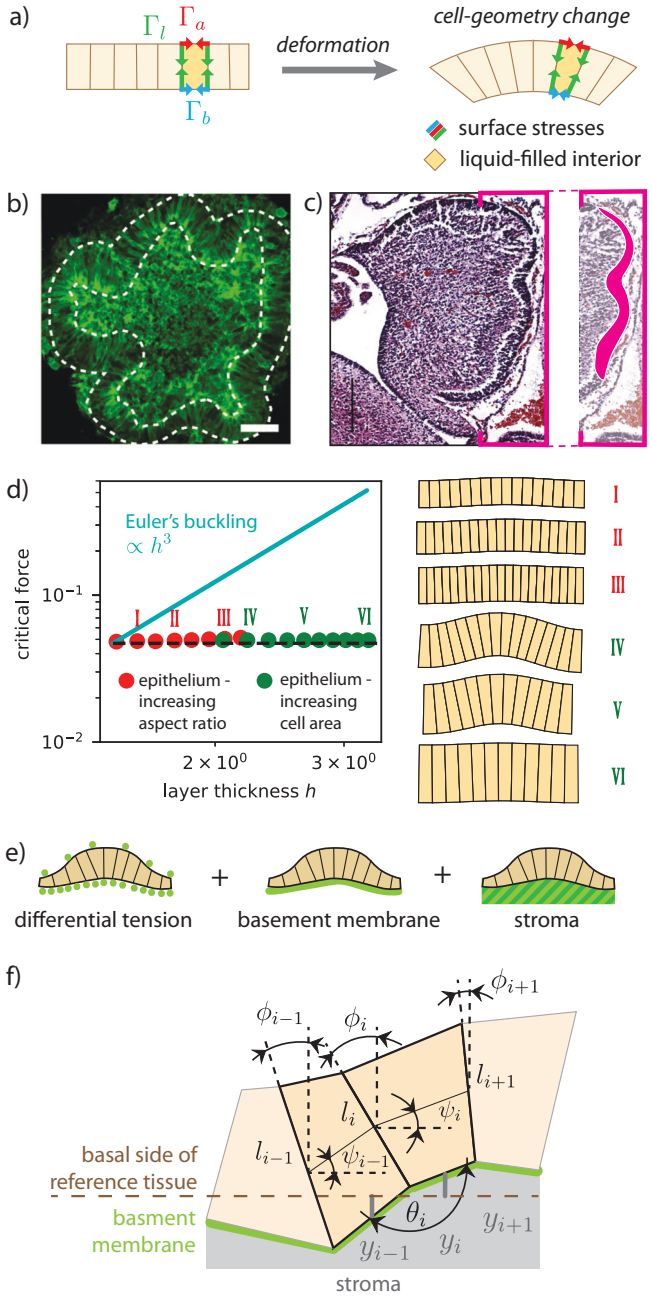

Fig. 1 | Vertex model of epithelial sheets. a Schematic of an epithelium, composed of liquid-filled cells with apical, basal, and lateral surface tensions Γ_a, Γ_b, and Γ_l, respectively. Only surface stresses of deformed cells contribute to the elastic energy. **b**,**c** Human brain organoid, reprinted from Fig. 4*a* in ref. 40 (**b** with scale bar 100μm) and midsaggital section of a mouse cerebellum, adapted from Fig. 5 in ref. 41 (**c**). Thickness modulation in both samples is in anti-phase compared to substrate undulations. Both Figures are reprinted with permission from Springer Nature. Contour in (**c**) was added to the original image. **d** Critical buckling force as a function of tissue thickness. Red and green data points show the results from the vertex model, whereas the cyan line is the result for the classic Euler's buckling of a plate. Right: Shapes of uniaxially compressed epithelia for different cell aspect ratios and cell-areas. **e** Schematics of contributions to the effective elastic energy: apico-basally polar surface tension marked with green dots (left), thin basement membrane marked with green line (middle), and elastic stroma marked with green area (right). **f** Detailed geometry of two adjacent cell cross-sections. Lateral edges are denoted by l_{i-1}, l_i, and l_{i+1}, azimuthal angles by ψ_i and ψ_{i+1}, lateral angles by ϕ_{i-1}, ϕ_i, and ϕ_{i+1}, basal angle by θ_i, and vertical displacements of the mid-point of basal edges y_i and y_{i+1}.

structure. Within the analogy with incompressible droplets, tissue deformations would contribute to an elastic energy, associated only with shape changes of cell outlines, whereas cell interiors would not support bulk elastic stresses (Fig. 1a)[25,26].

Experimentally, the relevance of surface tensions in epithelial mechanics may be underscored through a simple dimensional analysis where cell surface energy is compared with the bulk elastic energy, $\gamma L^2 \sim EL^3$. This comparison yields the elastocapillary length scale $\xi \sim \gamma/E$, representing a linear cell dimension below which surface tensions dominate over bulk elastic forces. Depending on cell type and various measurements, ξ is estimated to range between 0.1 and 10 μm[27–29]. Given that linear dimensions of epithelial cells are typically around $1 - 10$ μm, surface forces at the cell level should be considered in the coarse-grained picture of tissue elasticity. While a complete theoretical description of epithelial mechanics would incorporate both effects, the extent to which elastic properties of tissues may depart from those of nonliving elastic sheets due to surface-tension effects is here studied by a minimal model that assumes droplet-like mechanics of cells while entirely disregarding bulk elasticity.

The specific tension-dominated mechanics may result in tissues' unique large-scale elastic properties and deformations[30–33]. Epithelial layers consisting of droplet-like cells may exhibit unexpected behaviors such as forming wrinkles even when not being supported by substrates and features of shape may significantly differ from the analogous shapes in solid plates[34,35]. One such feature is the epithelial thickness modulation and its phase relative to the undulation of the epithelium-substrate interface: While in supported solid plates the thickness modulation is universally in phase with substrate undulations[13], an inverted phase is observed in some epithelia organoids (Fig. 1b, c), as well as in epithelia grown on wrinkled substrate[36–38]. Such phase-inverse cannot be explained within the classical elasticity theory[39–41] and cell surface tensions could be the root origin of the modulation[24,36,37,42–44].

In addition, the distinct epithelial elasticity may show up in unusual scaling relations of some of the key physical quantities such as the critical load to induce an elastic instability. This is suggested by a discrete model of uniaxially compressed epithelial monolayers, where apical, basal, and lateral cell sides are under constant surface tensions Γ_a, Γ_b, and Γ_l, respectively, while cells' interiors are assumed filled with an incompressible fluid. Using this model, we show that the critical buckling force is independent of the layer's thickness (Fig. 1d), in contrast to the classic Euler buckling of solid plates, where the critical force scales with thickness as $\propto h^3$. While the dependence of buckling threshold on cells' thickness has not yet been systematically studied, recent experiments show that a monolayer of epithelial cells exhibits the same buckling threshold as a stratified tissue and that the threshold depends strongly on cortical contractility[45]. These suggested deviations from predictions of the classical elasticity theory highlight a need to derive elasticity theories of tissues by coarse-graining their specific microscopic mechanics models rather than a priori assuming certain macroscopic elasticity.

Here, we address this challenge, by deriving an elasticity theory, describing epithelia supported by the basement membrane and the stroma (Fig. 1e). To explore the role of surface stresses in shaping the tissue, we assume that cell mechanics are dominated by surface tensions, while cell interiors resemble an incompressible fluid. We find that due to these specific mechanics, the coarse-grained elasticity is fundamentally different from classic supported solid plates. In particular, we study linear stability of flat tissues and explore conditions under which epithelia wrinkle or buckle out of plane. Importantly, our theory captures the unconventional scaling of the critical in-plane force to induce an elastic instability with epithelial thickness and shows that other key physical parameters such as the wavelength of wrinkles also scale differently than in supported solid plates. Finally, our approach naturally describes the phase inversion of the groove-to-crest thickness modulation and it offers a set of experimentally testable analytical results that may help uncover the relative contribution of surface mechanics to epithelial elasticity.

Results

Discrete cell-scale model

We study epithelial sheets in two dimensions, where we view them as chains of quadrilateral cell cross-sections. Cell interiors are assumed incompressible, meaning that the cross-section area of each cell is kept fixed at A_0. Cells adhere to their immediate neighbors along the lateral sides, whereas at the basal sides they are supported by a thin layer of extracellular material, i.e., the basement membrane (BM), and a thick stroma (Fig. 1f and Supplementary Note 1). Both BM and the stroma are considered elastic, carrying the bending- and bulk-elastic energy, respectively.

The apical, basal, and lateral cell sides are exposed to different microenvironments and carry distinct physiological functions, thereby being subjected to differential surface tensions. These tensions, denoted by Γ_a, Γ_b, and Γ_l for apical, basal, and lateral sides, respectively, result from cell-cell- and cell-substrate adhesion, and cortical tension due to acto-myosin contractility. In discrete form, the total potential energy of the entire epithelium-BM-stroma system is thus calculated as a sum over all cells and reads

$$W = \sum_i \left(\Gamma_a \ell_i^a + \Gamma_b \ell_i^b + \Gamma_l l_i + \frac{B}{2}\frac{\overline{\ell}_i^b}{\rho_i^2} + \frac{\overline{K}}{2} y_i^2 \ell_i^b \right). \tag{1}$$

Here ℓ_i^a, ℓ_i^b, and l_i are lengths of apical, basal, and lateral cell sides, respectively, ρ_i is the local radius of curvature of BM, evaluated at the basal vertex of $i-$th lateral side, whereas y_i is the vertical displacement of the midpoint of basal edge with index i from its reference position (Fig. 1f and Supplementary Note 1). In Eq. (1), the elastic-energy densities of BM and the stroma are multiplied by the corresponding basal lengths $\overline{\ell}_i^b = (\ell_{i-1}^b + \ell_i^b)/2$ and ℓ_i^b, respectively; B and $\overline{K}$ are the elastic moduli associated with BM's bending- and stroma's bulk-elastic deformations, respectively. To describe the contribution from the stroma within the linear-stability analysis, the bulk-elastic modulus $\overline{K}$ needs to be assumed proportional to the wavenumber of the dominant deformation mode (i.e., $\overline{K} = Kq$)[18].

We introduce dimensionless quantities by expressing lengths and tensions in units of $\sqrt{A_0}$ and Γ_l, respectively. In particular, we apply the following renormalizations: $l_i/\sqrt{A_0} \to l_i$ (and analogously for the other quantities with units of length), $W/(\Gamma_l\sqrt{A_0}) \to W$, $B/(\Gamma_l A_0) \to B$, and $K\sqrt{A_0}/\Gamma_l \to K$, and we define dimensionless average and differential apico-basal surface tensions as

$$\Gamma = \frac{\Gamma_a + \Gamma_b}{\Gamma_l} \quad \text{and} \quad \Delta = \frac{\Gamma_a - \Gamma_b}{\Gamma_l}, \tag{2}$$

respectively. Since we assume homogeneous monolayers, the values of Γ, Δ, K, and B are uniform along the tissue and, therefore, they are the only free parameters of our model.

Reference state. In a flat configuration, all cells assume rectangular shapes and the energy (Eq. (1)) per cell simplifies to $W/N = \Gamma/h + h$, where h is the cell height. Minimizing W with respect to h yields the optimal height

$$h = \Gamma^{1/2}. \tag{3}$$

Continuum limit

To derive a continuum limit of W (Eq. (1)), we first express apical and basal edge lengths and the local radius of curvature in Eq. (1) as functions of the lateral-side lengths l_{i-1}, l_i, and l_{i+1}, inclinations of cell midlines relative to the x-axis ψ_i and ψ_{i+1}, and the inclinations of lateral sides relative to the y-axis ϕ_{i-1}, ϕ_i, and ϕ_{i+1}. We treat these variables as well as y_i and y_{i+1} as functions of the distance σ along the reference-state midline: $\phi_i \to \phi(\sigma)$ and $\phi_{i+1} \to \phi(\sigma) + \dot{\phi}(\sigma)\sigma_0 + \ddot{\phi}(\sigma)\sigma_0^2/2$, where the "dot" denotes the derivative with respect to σ, and analogously for the other variables (Supplementary Note 1).

Next, we express the energy as an integral $L = \int_0^{Nh^{-1}} \mathcal{L}(\sigma)d\sigma$, where the Lagrangian density

$$\mathcal{L} = \mathcal{L}_T + \mathcal{L}_B + \mathcal{L}_K + \mathcal{L}_{C1} + \mathcal{L}_{C2} \tag{4}$$

is expanded to second order in the variables, $\delta l(\sigma) = l(\sigma) - h$, $\psi(\sigma)$, $\phi(\sigma)$, and $y(\sigma)$, describing deformations from the reference state, characterized by $\delta l = \psi = \phi = y = 0$. To simplify the equations, we hereafter omit the notation "δ" from $\delta l(\sigma)$ and its derivatives. The five terms in the Lagrangian density (Eq. (4)) are outlined below and derived in full details in Supplementary Note 1.

Epithelial **surface energy**, captured by the first three terms of Eq. (1), in continuum limit reads

$$\begin{aligned}\mathcal{L}_T = &\frac{\Delta \ddot{l}\ddot{\psi}}{8h^3} + \frac{\ddot{l}^2}{8h^4} + \frac{(4\ddot{l}l + \ddot{\psi})^2 - \ddot{\psi}\ddot{\phi} + \ddot{\phi}^2}{8h^2} + \\ &+ \frac{2\Delta\dot{l}\dot{\psi} + 2\dot{\psi}\ddot{\psi}}{4h} + h^2\left(\frac{1}{4}\dot{l}^2 + \psi^2 - 2\psi\phi + \phi^2 + 4\right) + \\ &+ \frac{1}{16}(\ddot{l}^2 + 16\Delta\psi\dot{l} + 32l^2 - 8\psi\ddot{\phi} - 8\dot{\psi}\dot{\phi} - 8\phi\ddot{\psi}) + \\ &+ h(\dot{\psi}(\psi - \phi) - \Delta\dot{\phi}).\end{aligned} \tag{5}$$

The **BM bending energy** expresses as an effective epithelial bending energy,

$$\mathcal{L}_B = \frac{B}{2}\left(\dot{\psi} - \frac{\ddot{l}}{2}\right)^2, \tag{6}$$

with $\ddot{l}/2$ playing the role of a local epithelial spontaneous curvature.

The term representing the **bulk elastic energy of the stroma** reads

$$\mathcal{L}_K = \overline{K}\,\frac{(\ddot{y} + 2h\dot{y} + 2hy)^2 + 4h^4y^2}{16h^4}. \tag{7}$$

Here, the variable y is, in fact, a dependent integral quantity given by $y(\sigma) = \int_0^\sigma s(t)\sin\psi(t)dt$, $s(t)$ being the tissue midline. By differentiating this expression with respect to σ, we obtain a constraint $\dot{y} = \psi - \dot{l}/2$, which is taken into account by the following term in the Lagrangian density:

$$\mathcal{L}_{C1} = Q(\sigma)h\left(\frac{\dot{l}}{2} - \psi + \dot{y}\right), \tag{8}$$

$Q(\sigma)$ being the corresponding Lagrange multiplier.

We study epithelial sheets under a small uniaxial compressive strain $|\epsilon| \ll 1$, imposed by a constraint $Nh^{-1}(1-\epsilon) = \int_0^{Nh^{-1}} \dot{x}d\sigma$, where x is the local projection of tissue midline to the horizontal axis. In the Lagrangian density, this constraint is represented by

$$\mathcal{L}_{C2} = \mu(1 - \epsilon - \dot{x}), \tag{9}$$

where μ is the applied load ensuring a fixed compressive strain ϵ. The variable $\dot{x}(\sigma)$ is derived from a local constraint of fixed cell-cross-section area.

The Lagrangian in Eq. (4) generalizes the model of ref. 34 by incorporating an elastic interaction between the tissues and the substrate. This extension yields a more comprehensive coarse-grained elasticity theory, enabling a detailed study of the interplay between cell surface tensions and substrate elasticity, and allowing us to address elastic instabilities, critical buckling forces, compression, and thickness profiles in this, more complete, setting.

Throughout the text, the analytical results are compared with the results of vertex-model simulations that minimize the discrete model (Eq.

(1)) in its full non-linear form (Materials and Methods). In all figures, the results of the vertex model are denoted by datapoints, whereas the analytical results are represented by solid curves.

Deformation modes

The Lagrangian yields a system of three differential equations for variables $\psi(\sigma)$, $\phi(\sigma)$, and $l(\sigma)$ (Supplementary Note 2). We solve it in the Fourier space by assuming $\psi(\sigma) = \int \Psi(q)\exp(\mathrm{i}q\sigma)\mathrm{d}q$, $\phi(\sigma) = \int \Phi(q)\exp(\mathrm{i}q\sigma)\mathrm{d}q$, and $l(\sigma) = \delta h + \int \Lambda(q)\exp(\mathrm{i}q\sigma)\mathrm{d}q$, q being the wavenumber of deformation mode and $\delta h \ll h$ a constant part of cell-height deformation. Upon these transformations, the system of governing equations simplifies to a single polynomial equation, which is solved to obtain the force μ as a function of the wavenumber q. At the onset of instability (i.e., at small μ and q), we obtain

$$\begin{aligned}\mu = &\frac{K}{q} + \frac{K(h^4 + 2h^2\Delta - 2)q}{8h^2} + \\ &+ \frac{(8B - \Delta^2 + 2)q^2}{8} + \frac{K(h^4+5)q^3}{16h^4} + \\ &+ \frac{[8B(h^4/2 + h^2\Delta - 1) + h^4 - \Delta^2]q^4}{32h^2}\,.\end{aligned} \tag{10}$$

By comparing this equation to its analogue for nonliving supported thin sheets (e.g., ref. 18), we extract the effective bending modulus of the epithelium-BM bilayer from the quadratic term: $B_{\mathrm{eff}} = B + (2 - \Delta^2)/8 \propto h^0$. This modulus can either be negative or positive, depending on the Δ-value, indicating an elastic instability. While B_{eff} does not depend on thickness, the effective Young's modulus, calculated in ref. 34, scales with thickness as $E \propto h^2$. Both moduli scale differently than in solid plates and so does their ratio $B/E \propto h^{-2}$. Other related studies that mostly coarse grain 2D vertex models with area and perimeter elasticity–where tissues are represented as planar polygonal tilings–have also reported unusual elastic moduli[46–49]. However, since the reduced-dimensionality 2D vertex models do not describe cell height, their effective elastic moduli do not yield scaling with h.

Buckling. Since the total deformation energy equals the work of the applied load $\int_0^{Nh^{-1}} \mu d\sigma$, the dominant deformation mode at the point of instability is characterized by q_0, where $(\partial\mu/\partial q)_{q=q_0} = 0$. Depending on Γ, Δ, B, and K, tissues undergo either buckling or wrinkling instability, where $q_0 = 0$ ($q_0 = 2\pi/L$ for tissues with finite end-to-end length L) or $q_0 > 0$, respectively. In absence of the apico-basal differential tension (i.e., $\Delta = 0$) and supporting structures (i.e., $B = K = 0$), a tissue with an end-to-end length L buckles at a critical force $\mu_0 = \pi^2/L^2 \propto h^0$ (Supplementary Notes 3 and 4). This result agrees with numerical results (Fig. 1d) and is in contrast with Euler instability in solid plates, where $\mu_c \propto h^3$.

The critical buckling force is related to the critical compressive strain by (Supplementary Note 3)

$$\mu_c = 2h^2\epsilon_c\,, \tag{11}$$

such that in absence of differential tension and supporting structures,

$$\epsilon_0 = \frac{\pi^2}{2h^2L^2} \propto h^{-2}\,. \tag{12}$$

Interestingly, while ϵ_0, like μ_0, is inversely proportional to the length squared (i.e., $\epsilon_0 \propto L^{-2}$), similarly to the standard Euler instability in solid plates, the h^{-2}-dependence on the layer thickness in Eq. (12) is, again, fundamentally different from the h^2-dependence in plates (Fig. 2a).

Buckling persists when the tissue is supported by BM, however, the critical compressive strain increases relatively to the unsupported case and reads $\epsilon_0(1 + 4B)$. In contrast, the apico-basal differential tension Δ tends to decrease the critical compressive strain as $\epsilon_0(1 - \Delta^2/2)$. At $\Delta = \sqrt{2}$, where the tissue transitions from buckling to wrinkling, as discussed in the next section, the critical compressive strain is 0.

Tissues with non-zero differential tension which are additionally supported by a BM (i.e., $\Delta \neq 0$ and $B > 0$), buckle once the compressive strain reaches a critical value (Fig. 2b)

$$\epsilon_{\mathrm{c,buck}}^{[\Delta,B]} = \epsilon_0\left(1 - \frac{\Delta^2}{2} + 4B\right), \tag{13}$$

which includes both individual contributions of Δ and B.

Buckling-to-wrinkling transition. The competing effects of the combined tissue-BM bending rigidity and the apico-basal differential tension result in a transition from buckling to wrinkling, whereby an initially flat tissue becomes contractile and it spontaneously loses stability at a periodic mode, characterized by a wavenumber q_0, which minimizes μ (Eq. (10)).

The contractile behavior of the tissue is seen in a negative critical compressive strain for $|\Delta|$ above the wrinkling threshold (Fig. 2c)

$$\Delta_c^{[B]} = \sqrt{2(1 + 4B)}\,, \tag{14}$$

where

$$\epsilon_{\mathrm{c,wrink}}^{[\Delta,B]} = -\frac{4B + 1}{2(h^4 - 2)}\left(|\Delta| - \Delta_c^{[B]}\right)^2. \tag{15}$$

In absence of BM (i.e., $B = 0$), the critical differential tension reduces to $\Delta_c = \sqrt{2}$, which agrees with the result previously derived for unsupported tissues[34]. Note that here, both $\epsilon_{\mathrm{c,wrink}}^{[\Delta,B]}$ and $\mu_{\mathrm{c,wrink}}^{[\Delta,B]} = 2h^2\epsilon_{\mathrm{c,wrink}}^{[\Delta,B]}$ scale differently with the thickness h compared to the buckling regime (Fig. 2a).

Wrinkling. For $|\Delta| > \Delta_c^{[B]}$, tissues develop periodic wrinkling patterns, characterized by a wavenumber (Fig. 2d)

$$q_0^{[\Delta,B]} = \frac{2^{5/4}}{\sqrt{h^2 - 2/h^2}}\left(|\Delta| - \Delta_c^{[B]}\right)^{1/2}. \tag{16}$$

The presence of the stroma causes wrinkling regardless of the presence of BM and the differential surface tension, i.e., the optimal wavenumber q_0 is always non-zero and the divergence in denominator is only apparent since $\sqrt{2} < \Delta < h^2$. When considering only the effects of the stroma and neglecting both the differential surface tension and the interaction with BM (i.e., $\Delta = B = 0$), the corresponding governing equations yield a critical wrinkling compressive strain

$$\epsilon_c^{[K]} = 3 \cdot 2^{-7/3}h^{-2}K^{2/3} \propto h^{-2} \tag{17}$$

and a critical force $\mu_c^{[K]} = 3 \cdot 2^{-4/3}K^{2/3} \propto h^0$ with a dominant wrinkling mode, given by a wavenumber (Fig. 2e)

$$q_0^{[K]} = (2K)^{1/3} \propto h^0\,. \tag{18}$$

Scaling relations of ϵ_c, μ_c, and q_0 with K are the same as in supported solid plates, but the scaling of all three quantities with thickness h is fundamentally different. Indeed, in solid plates, $\epsilon_c \propto h^0$, $\mu_c \propto h$, and $q_0 \propto h^{-1}$[50].

In tissues supported by stroma, where, additionally, the effects of Δ and B are present, we examine the optimal wavenumber perturbatively. Since K in Eq. (10) appears at the lowest order in q, its influence is greater than that of Δ and B, which is why we can treat corrections due to Δ and B perturbatively as $q_0^{[\Delta,B,K]} = q_0^{[K]} + \delta q(\Delta, B, K)$, where $\delta q(\Delta, B, K) \ll q_0^{[K]}$. For small Δ and

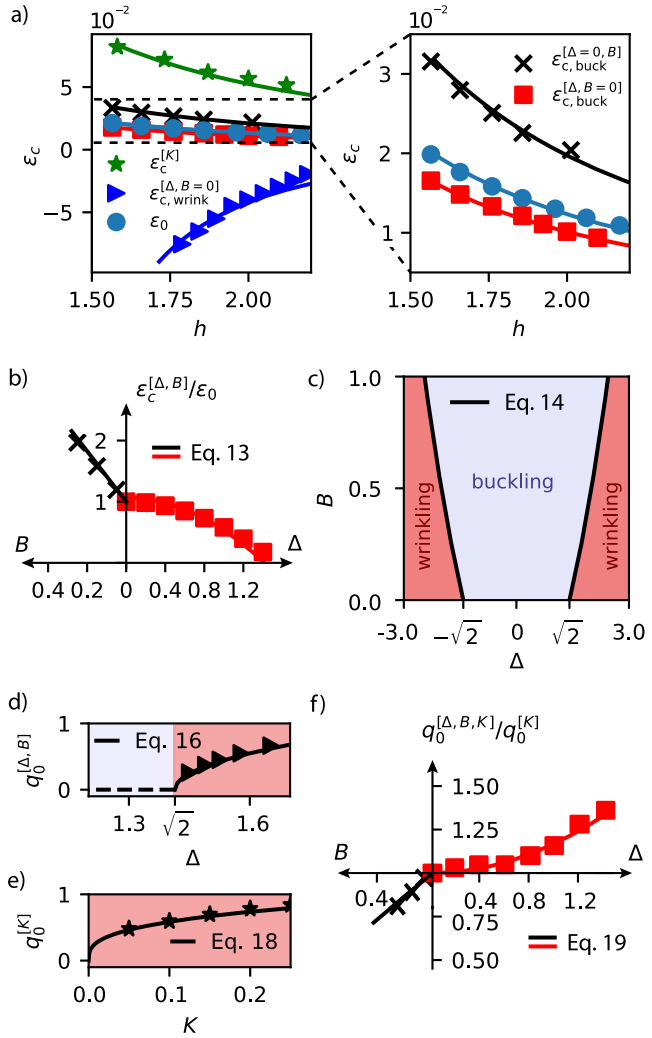

Fig. 2 | Instability analysis in epithelial sheets. a Critical compressive strain ϵ_c of the epithelium in different limits: Unsupported epithelium with non-polar surface tensions (ϵ_0, blue dots), epithelium, supported by BM ($\epsilon^{[B]}$, black crosses), epithelium, supported by stroma ($\epsilon^{[K]}$, green stars), and epithelium with differential surface tension ($\epsilon^{[\Delta]}_{\text{buck}}$ in red squares and $\epsilon^{[\Delta]}_{\text{wrink}}$ in blue triangles for buckling and wrinkling deformation mode, respectively). The left panel contains both buckling and wrinkling regimes, while only the buckling regimes are present on the right panel. **b** Relative critical compressive strain ϵ for buckling instability as a function of B (black) and Δ (red); $\Gamma = 3.5$. **c** Phase diagram $B(\Delta)$ showing regions of buckling and wrinkling. **d** Wavenumber of wrinkling in an unsupported epithelium ($B = K = 0$) as a function of Δ for $\Gamma = 4$. **e** Wavenumber of wrinkling in an epithelium supported by the stroma as a function of K for $\Delta = B = 0$ and $\Gamma = 4$. **f** Relative optimal wavenumber of wrinkling patterns, $q_0^{[K,\Delta,B]}$, as a function of B (black) and Δ (red); $\Gamma = 3.5$ and $K = 0.1$. In all panels, datapoints represent vertex-model results, B denotes the bending modulus of the basement membrane, K denotes the elastic modulus of the stroma, and Δ denotes the apico-basal differential surface tension. In **c**–**e**, red color denotes wrinkling regime and purple denotes buckling regime.

B, we obtain

$$q_0^{[\Delta,B,K]} = q_0^{[K]}\left(1 + \frac{1}{6}[\Delta^2 - 8B]\right). \tag{19}$$

This result shows that BM's bending rigidity increases the wavelength while $|\Delta|$ decreases it (Fig. 2f). The asymmetry between positive and negative Δ-values due to basal presence of the substrate enters q_0 at the next lowest order (Supplementary Note 4). Note that because Eq. (19) was obtained perturbatively for small deviations of the wavenumber from $q_0^{[K]}$, assuming small Δ- and B-values, it does not reduce to Eq. (16) for $K = 0$.

Thickness modulation

The characteristic wavelength of the deformation pattern is often the primary geometric observable in deformed multilayered elastic sheets and can be used to determine the relative stiffnesses of the layers. However, our results show that the elastic interaction among the layers may not always be the dominant mechanism of wrinkling, since wrinkling can also appear in unsupported sheets due to specific internal forces, namely differential interfacial tensions. As a result, the wrinkling wavelength may not be the sole and most reliable observable to pinpoint the dominant mechanism of wrinkling in soft biological tissues.

An additional shape feature of interest is the groove-to-crest modulation of the layer thickness. Indeed, in supported solid plates, the thickness is modulated along the waveform and this modulation is universally *in phase* with the undulation of the layer-substrate interface, such that the top (thin) layer is thicker in crests than in grooves[13,51,52]. In various elastic bilayers, the thickness modulation of the thinner film is often not explored or it is modeled to be constant[53–56]. The inverted thickness modulation (i.e., the thickness modulates in *anti-phase* with substrate undulations) (Fig. 3a) has been so far experimentally observed in certain organoid systems[39] and epithelia, grown on wavy substrates[37,38] as well as theoretically predicted for epithelia with non-negligable effects of surface tension[24,34] and due to the presence of system-spanning elastic fibers, present in certain organs[39]. In non-living systems, a similarly unusual thickness modulation has been reported in elastic three-layered composite, where the wrinkling pattern of the thin middle layer transitions from serpentines to pearling[57].

Our model suggests that the phase inversion may naturally emerge from the surface mechanics at the cell level. In particular, close to the point of elastic instability, governing equations are solved by $l(\sigma) = \delta h + \Lambda\cos(q\sigma)$, $y(\sigma) = Y\cos(q\sigma)$, and $\psi(\sigma) = \Psi\sin(q\sigma) + \Psi_1\cos(q\sigma)$ (Supplementary Note 5). Together with Eq. [(8)], which connects the amplitudes by $Y = -\Lambda/2 - \Psi/q$, this solution allows a simple definition of thickness modulation, relative to the amplitude of substrate undulations:

$$\tau = \frac{\Lambda}{Y} \approx -\frac{q\Lambda}{\Psi}. \tag{20}$$

Its magnitude and the sign (phase) are calculated as $|\tau|$ and $sgn(\tau)$, respectively; τ is defined such that $sgn(\tau) = 1$ for tissues that are thicker in crests (i.e., thickness modulation and the stroma undulation are in phase), whereas $sgn(\tau) = -1$ for tissues thicker in grooves (i.e., thickness modulation and the stroma undulation are in anti-phase) (Fig. 3a).

The ratio of amplitudes Λ/Ψ and the wavenumber q follow directly from governing equations and are derived for different regimes in Supplementary Note 5. We find that while an unsupported tissue with no apico-basal polarity (i.e., $K = B = \Delta = 0$) exhibits no thickness modulation, i.e., $\tau = 0$, in any other case, the thickness is modulated and this modulation can either be in phase or in anti-phase with substrate undulations, depending on parameters (Fig. 3b, c).

In-phase thickness modulation. In presence of BM but absence of the stroma (i.e., $B \neq 0, K = 0$), the tissue with no apico-basal differential tension (i.e., $\Delta = 0$) bends such that $q^{[B]} = 2\pi/L$. In this case, the thickness modulation

$$\tau^{[B]} = \frac{4\pi^4 B}{L^4} > 0 \tag{21}$$

is always in-phase with substrate undulations (Fig. 4a).

When BM is absent but the epithelium is supported by the stroma (i.e., $B = 0, K > 0$), the tissue wrinkles and the thickness modulation

$$\tau^{[K]} = 2^{-5/3}K^{4/3} > 0 \tag{22}$$

is, again, in phase with substrate undulations (Fig. 4b).

Phase inversion. The modulation phase cen be inverted by the apico-basal differential surface tension Δ. In absence of supporting structures

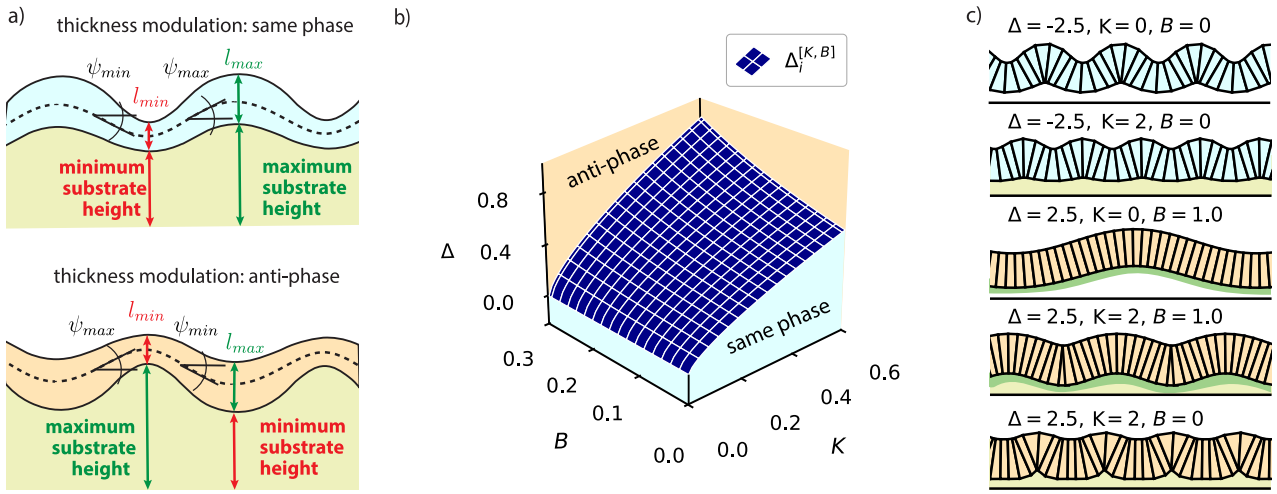

Fig. 3 | Thickness modulation phase. a Schematics of a tissue exhibiting thickness modulation in phase with substrate undulations (top) and a tissue exhibiting tissue modulation with opposite phase compared to substrate undulations (bottom). **b** Phase diagram $\Delta(B, K)$ showing regions of in-phase (cyan) and anti-phase (orange) thickness modulations; here, B is the bending modulus of the basement membrane, K is the elastic modulus of the substrate, and Δ is the apico-basal differential surface tension. The dark blue surface shows $\Delta_i^{[\Delta,B,K]}$, where the phase is inverted. **c** Examples of optimal tissue shapes obtained by vertex-model simulations. The cell color denotes whether the thickness modulation has the same phase as substrate undulations (blue) or an opposite phase (orange). In all simulations, $\Gamma = 4$.

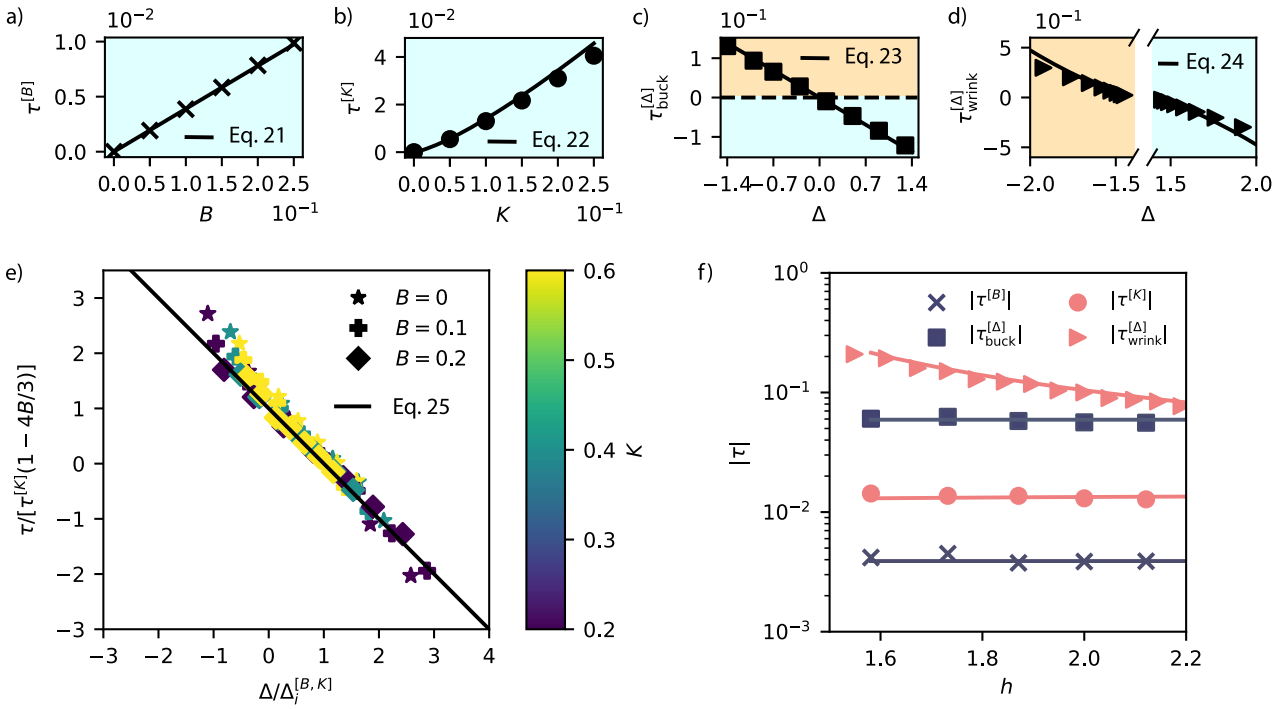

Fig. 4 | Thickness modulation in epithelial sheets. a,**b** Thickness modulation τ as a function of B and K in the limit of no differential tension and only BM and stroma present (**a** and **b**, respectively). **c**,**d** Thickness modulation τ as a function of Δ in the limit of no substrate present in the buckling and the wrinkling regime (**c** and **d**, respectively). In **a**–**d**, $\Gamma = 4$ and blue and orange areas represent same-phase and anti-phase modulation, respectively. **e** Comparison of analytical expression for thickness modulation (solid line) and numerical results of vertex model simulations in tissues with $B = 0, 0 < K < 0.1, -0.1 < \Delta < 0.3$, and $\Gamma = 4$. **f** Comparison of thickness modulation amplitudes $|\tau|$ in tissues of similar length with different supporting structures. Parameter values are $B = 0.1$ for $\tau^{[B]}$ (dark blue crosses), $K = 0.1$ for $\tau^{[K]}$ (brick circles), $\Delta = 0.6$ for $\tau^{[\Delta]}_{\text{buck}}$ (dark blue squares), and $\Delta = 1.6$ for $\tau^{[\Delta]}_{\text{wrink}}$ (brick triangles). Dark blue and brick colors represent buckling and wrinkling modes, respectively. In all panels, datapoints represent vertex-model results, B is the bending modulus of basement membrane, K is the elastic modulus of the stroma, and Δ is the apico-basal differential surface tension.

(i.e., $B = K = 0$), the modulation, caused by Δ, differs between buckling and wrinkling. In a buckled tissue of end-to-end length L, it reads

$$\tau^{[\Delta]}_{\text{buck}} = -\frac{\pi^2 \Delta}{L^2} \gtrless 0\,, \tag{23}$$

whereas in a wrinkled tissue

$$\tau^{[\Delta]}_{\text{wrink}} = -\frac{\sqrt{2}\Delta(|\Delta|-\sqrt{2})}{h^2-2/h^2} \gtrless 0\,. \tag{24}$$

In both deformation regimes, the value of τ can be either positive or negative and the phase in both cases changes at $\Delta = \Delta_i^{[\Delta]} = 0$ (Fig. 4c, d).

The phase inversion can be intuitively understood by observing the size of apical and basal tissue surfaces in in-phase and in anti-phase configurations (Fig. 3a): When thickness modulation is in phase with substrate undulations, the apical area is larger than the basal, whereas the opposite is true in anti-phase configurations. Tissues can, thus, invert the modulation phase by increasing the apical tension, thereby decreasing their apical surfaces.

An inverse of modulation phase can occur even in the presence of supporting structures. While the combined effects of the differential surface tension, BM, and the stroma cause the tissue to wrinkle with a wavelength, predominantly determined by the stiffness of the stroma (Eq. (19)), the associated thickness modulation,

$$\tau^{[K,\Delta,B]} = \tau^{[K]}\left(1-\frac{4}{3}B-\frac{2^{1/3}\Delta}{K^{2/3}}\left[1-\frac{4}{3}B\right]^2\right), \tag{25}$$

is primarily set by the differential surface tension. In particular, thickness modulation inverts its phase when τ switches sign, which occurs when the apico-basal differential surface tension exceeds a transition value

$$\Delta_{\mathrm{i}}^{[B,K]} = \frac{2^{-1/3}K^{2/3}}{1-4B/3}, \tag{26}$$

which is entirely determined by elastic properties of the substrate, i.e., BM and the stroma (Fig. 3b and Fig. 4e). Note that, similarly to Eq. (19), Eq. (25) is only valid for small B and Δ (Supplementary Note 5).

In terms of the contribution of various effects to the thickness-modulation amplitude, $|\tau|$, Fig. 4f confirms that the effect of the differential tension is much higher than the effects of the interaction of tissue with either BM or the stroma. Additionally, the thickness-modulation amplitude depends on the layer's baseline thickness h only when the modulation is caused by the apico-basal differential tension, sufficient to drive tissue wrinkling (Fig. 4f and Eqs. (21)–(24)).

Our model assumes that the tissue can freely slide along the substrate and can, therefore, be readily used to describe the shape of tissues grown on stiff wavy support[36,38]. We can rewrite Eq. (18) to express the modulus K as a function of deformation wavenumber $q = 2\pi/\lambda$ and, using Eq. (25) for $B = 0$, express thickness modulation as $\tau^{[\lambda,\Delta]} = -\Delta\pi^2\lambda^{-2} + 2\pi^4\lambda^{-4}$, where λ is the pre-determined wavelength of substrate undulations. This result agrees with the measurements in refs. 36,38 and could be used to estimate the differential tension Δ directly from the height modulation. Such study would require more detailed height measurements for different substrate wavelengths to distinguish between the applicability of our theory and other alternative models[36,38].

Discussion

We developed an elasticity theory for epithelial tissues supported by the basement membrane and the stroma. Unlike most existing theories, which assign specific elastic properties to the epithelium[19,21], our approach derives these properties from a microscopic, cell-scale model based on differential interfacial tensions. By adopting a simplified mechanical framework that treats cells as incompressible droplets with stresses localized at their surfaces, we examined the influence of interfacial surface tensions on epithelial elasticity.

We compared the results with the classic elasticity of solid plates, where stresses are distributed throughout the volume, and identified several key differences, summarized in Table 1. Firstly, while classic thin plates wrinkle only when supported by a thick substrate, epithelia may wrinkle due to finite-thickness effects and the associated apico-basal tension asymmetry even in absence of substrate. Secondly, the different origin of elasticity results in specific scaling relations of the wavenumber as well as the critical buckling/wrinkling force and compressive strain with layer thickness. In our model, thickness is varied by varying cells' aspect ratio while maintaining fixed cell cross-section areas, however, the same scaling relations are obtained in a scenario where the height is varied by varying the area while fixing the aspect ratio (Supplementary Note 6). Finally, deformed epithelial monolayers exhibit modulation of thickness that is either in phase or in anti-phase with undulations of the epithelium-substrate interface. While the in-phase modulation is not surprising[13], the anti-phase modulation is, since it is not present in classic supported solid plates and has been only recently observed in epithelial monolayers[36,38,39]. Importantly, our model predicts that the anti-phase modulation may only arise when the apical tension is greater than the basal tension.

The predicted anomalous elastic properties and deformations of epithelia highlight the need for experimental validation. Several experiments suggest the epithelial tissues have unusual elasto-mechanical properties[30,37,38,45]. For instance, in ref. 45 the authors observe that a single-layered epithelium exhibits the same buckling threshold as a thicker stratified tissue. While this experiment does not describe exactly the setup assumed in our theory (i.e., a monolayer of varying thickness), it indicates that the critical buckling force may be affected by the specific microscopic cell interactions and the standard theory of plate elasticity may not be sufficient. The same experiments observe that the effective epithelial stiffness can be altered by regulators of contractility by one order of magnitude without noticeable changes in cellular junctional network, suggesting that the contractile behavior of cell cortices, similar to the one incorporated here through surface tensions, should be considered when modeling tissue's elasticity[58].

In this study, we analyzed a minimal model of supported monolayers where (constant) surface tensions dominate over bulk elasticity of cells and we leave the exploration of more advanced models for future work. We have neglected cells' bulk elasticity[27–29] in order to emphasize the contribution of surface mechanics to emergent elasticity as clearly as possible. Aside from living tissues, where bulk elasticity may play an important role as elaborated in Introduction, our theory could readily be tested in systems where entirely neglecting bulk elasticity is more directly justifiable. Some examples include sheets of adherent lipid vesicles or non-biological sheets composed of immiscible microfluidic droplets[59,60]. In these setups, differential surface tensions could be controlled by anchoring the sheets at interfaces between immiscible liquids or by introducing surfactants to modulate interfacial properties. Together with the insights from our theory, these proposed experiments may prove useful within a broader field of the study of soft metamaterials, which seeks to understand how design properties at smaller scales influence emergent elastic properties at the system level. Within this context, our theory highlights that microscopic interactions can have a profound impact on the overall properties, deformations, and shapes of elastic sheets, which may exhibit behaviors distinct from conventional elastic layers due to the unique microscopic origins of their elasticity.

Our current theory can be generalized to include mechano-chemical feedback[61–63] as well as space- and deformation-dependent surface tensions. Further on, while single-cell-volume remains constant during many events that include drastic tissue deformations, such as gastrulation[64] or furrowing[65], it can change considerably in contact with different substrates[66,67] or spontaneously oscillate[68,69]. In Supplementary Note 7, we generalize our model to include cell compressibility. We find that the results remain qualitatively the same as in the case of incompressible cells: We observe buckling-to-wrinkling transition as well as unusual scaling of buckling threshold with tissue thickness. Finally, the future work will need to include the effects of cells' bulk elasticity, as well as more rigorously include three-dimensional effects[58], and study large deformations, where non-linear contributions may play an important role[9,18,70].

Methods

Vertex model

Our vertex model describes the tissue as a chain of quadrilateral cell cross sections. The basal, apical, and lateral edges of cell i are under tensions Γ_{b}, Γ_{a}, and Γ_{l}, respectively, and their lengths are denoted by ℓ_i^b, ℓ_i^a, and l_i, respectively. Additionally, the tissue is supported by a basement membrane (BM) with a bending rigidity B and the stroma with a bulk elastic modulus $\overline{K}$. The

Table 1 | Comparison of our theory predictions with standard elastic (bi)layers

	supported epithelia	solid plates	supported solid plates
instability mode	buckling/wrinkling	buckling	wrinkling
wavenumber	$q = 2\pi/L$ for $K = 0$ & $\Delta < \Delta_c^{[B]}$ $q \propto (\Delta - \Delta_c^{[B]})^{1/2}$ for $K = 0$ & $\Delta > \Delta_c^{[B]}$ $q \propto K^{1/3}h^0$ for $K > 0$	$q = 2\pi/L$	$q \propto K^{1/3}h^{-1}$
critical force	$\mu_c \propto h^0 L^{-2}$ for $K = 0$ & $\Delta < \Delta_c^{[B]}$ $\mu_c \propto (\Delta - \Delta_c^{[B]})^2$ for $K = 0$ & $\Delta > \Delta_c^{[B]}$ $\mu_c \propto K^{2/3}h^0$ for $K > 0$	$\mu_c \propto h^3 L^{-2}$	$\mu_c \propto K^{2/3}h$
critical compressive strain	$\epsilon_c \propto h^{-2}L^{-2}$ for $K = 0$ & $\Delta < \Delta_c^{[B]}$ $\epsilon_c \propto (\Delta - \Delta_c^{[B]})^2$ for $K = 0$ & $\Delta > \Delta_c^{[B]}$ $\epsilon_c \propto K^{2/3}h^{-2}$ for $K > 0$	$\epsilon_c \propto h^2 L^{-2}$	$\epsilon_c \propto K^{2/3}h^0$
groove-crest thickness-modulation phase	in phase/in anti-phase with substrate undulations	N/A	in phase with substrate undulations
groove-crest thickness-modulation amplitude	$y_0 \times f(\Delta, B, K)$ (Eq. (25))	N/A	$\ll y_0$

dimensionless potential energy of the epithelium-BM-stroma system reads

$$e = \sum_i^N [\kappa_A (A_i - 1)^2 + \frac{\Gamma + \Delta}{2}\ell_i^a + \frac{\Gamma - \Delta}{2}\ell_i^b + \\ + l_i + \frac{B}{2}\rho_i^{-2}\frac{\ell_{i-1}^b + \ell_i^b}{2} + \frac{\overline{K}}{2}y_{i,b}^2\ell_i^b], \quad (27)$$

where ρ_i and $y_{i,b}$ denote the local curvature radius of the basement membrane and the y-coordinate of the basal vertex of i-th lateral edge, respectively. The cell-area modulus $\kappa_A = 100$, describes nearly incompressible cells with actual areas close to the preferred $A = 1$. All edge lengths and cell areas are calculated as $l_i = |\boldsymbol{r}_{i,\mathrm{head}} - \boldsymbol{r}_{i,\mathrm{tail}}|$ and $A_i = (1/2)\sum_\mu (\boldsymbol{r}_{i,\mu} \times \boldsymbol{r}_{i,\mu+1}) \cdot (0,0,1)$, respectively, where μ denotes a internal index of the cells, $\mu = 1 \ldots 4$, whereas the local squared curvature of the basement membrane is calculated as $\rho_i^{-2} = 8(1 + \cos\theta_i)/|r_{i+1,\mathrm{basal}} - r_{i-1,\mathrm{basal}}|^2$; the expression for angle θ_i is given in Supplementary Note 1. The energy is minimized using gradient descent, such that each vertex $\boldsymbol{r}_j = (x_j, y_j)$ moves with a velocity, proportional to the sum of conservative forces given by $\boldsymbol{F}_j = -\nabla_j e$.

In each simulation, we treat only one period of a periodic pattern, assuming periodic boundary conditions in the horizontal direction, such that N in e denotes the number of cells per waveform. Therefore, $q \approx 2\pi/L_0$, where $L_0 = Nh^{-1}$ is the initial length of the simulation box and, thus, $\overline{K} = 2\pi hK/N$. To find the optimal number of cells per waveform and the critical compressive strain, at which the elastic instability occurs, our simulations both vary the cell number N and the compressive strain $\epsilon = \delta L/L_0$ as well as simulate the descent of the system towards the minimum of e so as to find the exact optimal tissue shape.

Data availability

Processed simulation data used to generate the figures are available on Zenodo under accession code https://doi.org/10.5281/zenodo.18162163. Raw outputs are available upon request.

Code availability

The software used to compute all numerical data included in the manuscript is available on Zenodo under accession code https://doi.org/10.5281/zenodo.18162163.

Received: 13 May 2025; Accepted: 5 February 2026;
Published online: 24 February 2026

References

1. Rauzi, M., Verant, P., Lecuit, T. & Lenne, P.-F. Nature and anisotropy of cortical forces orienting drosophila tissue morphogenesis. *Nat. Cell Biol.* **10**, 1401–1410 (2008).
2. Collinet, C., Rauzi, M., Lenne, P.-F. & Lecuit, T. Local and tissue-scale forces drive oriented junction growth during tissue extension. *Nat. Cell Biol.* **17**, 1247–1258 (2015).
3. Rauzi, M. et al. Embryo-scale tissue mechanics during drosophila gastrulation movements. *Nat. Commun.* **6**, 8677 (2015).
4. Hubert, M. et al. Mechanical regulation of epithelial tissue homeostasis. *Phys. Rev. X* **11**, 031029 (2021).
5. Lecuit, T. & Lenne, P.-F. Cell surface mechanics and the control of cell shape, tissue patterns and morphogenesis. *Nat. Rev. Mol. Cell Biol.* **8**, 633–644 (2007).
6. Lecuit, T., Lenne, P.-F. & Munro, E. Force generation, transmission, and integration during cell and tissue morphogenesis. *Annu Rev. Cell Dev. Biol.* **27**, 157–184 (2011).
7. Shyer, A. E. et al. Emergent cellular self-organization and mechanosensation initiate follicle pattern in the avian skin. *Science* **357**, 811–815 (2017).
8. Timoshenko, S. & Gere, J.*Theory of Elastic Stability* (McGraw-Hill Book Co. Inc., 1961).
9. Pocivavsek, L. et al. Stress and fold localization in thin elastic membranes. *Science* **320**, 912–916 (2008).
10. Jiang, H. et al. Finite deformation mechanics in buckled thin films on compliant supports. *Proc. Natl. Acad. Sci. USA* **104**, 15607–15612 (2007).
11. Ben Amar, M. Wrinkles, creases, and cusps in growing soft matter. *Rev. Mod. Phys.* **97**, 015004 (2025).
12. Biot, M. A. Surface instability of rubber in compression. *Appl. Sci. Res.* **12**, 168–182 (1963).
13. Tallinen, T., Chung, J. Y., Biggins, J. S. & Mahadevan, L. Gyrification from constrained cortical expansion. *Proc. Natl. Acad. Sci. USA* **111**, 12667–12672 (2014).
14. Ackermann, J., Qu, P.-Q., LeGoff, L. & Ben Amar, M. Modeling the mechanics of growing epithelia with a bilayer plate theory. *Eur. Phys. J.* **137**, 8 (2021).
15. Savin, T. et al. On the growth and form of the gut. *Nature* **476**, 57–62 (2011).
16. Tallinen, T. et al. On the growth and form of cortical convolutions. *Nat. Phys.* **12**, 588–593 (2016).
17. Cerda, E. & Mahadevan, L. Geometry and physics of wrinkling. *Phys. Rev. Lett.* **90**, 074302 (2003).

18. Brau, F. et al. Multiple-length-scale elastic instability mimics parametric resonance of nonlinear oscillators. *Nat. Phys.* **7**, 56–60 (2011).
19. Shyer, A. E. et al. Villification: how the gut gets its villi. *Science* **342**, 212–218 (2013).
20. Amar, M. B. & Jia, F. Anisotropic growth shapes intestinal tissues during embryogenesis. *Proc. Natl. Acad. Sci. USA* **110**, 10525–10530 (2013).
21. Hannezo, E., Prost, J. & Joanny, J.-F. Instabilities of monolayered epithelia: shape and structure of villi and crypts. *Phys. Rev. Lett.* **107**, 078104 (2011).
22. Efimenko, K. et al. Nested self-similar wrinkling patterns in skins. *Nat. Mater.* **4**, 293–297 (2005).
23. Thompson, D. W.*On Growth and Form*. Canto (Cambridge University Press, 1992).
24. Riccobelli, D. & Bevilacqua, G. Surface tension controls the onset of gyrification in brain organoids. *J. Mech. Phys. Solids* **134**, 103745 (2020).
25. Derganc, J., Svetina, S. & Žekš, B. Equilibrium mechanics of monolayered epithelium. *J. Theor. Biol.* **260**, 333–339 (2009).
26. Hannezo, E., Prost, J. & Joanny, J.-F. Theory of epithelial sheet morphology in three dimensions. *Proc. Natl. Acad. Sci. USA* **111**, 27–32 (2013).
27. Wei, M.-T. et al. A comparative study of living cell micromechanical properties by oscillatory optical tweezers. *Opt. Express* **16**, 8594–8603 (2008).
28. Nussenzveig, H. M. Cell membrane biophysics with optical tweezers. *Eur. Biophys. J.* **47**, 499–514 (2018).
29. Fischer-Friedrich, E., Hyman, A. A., Jülicher, F., Müller, D. J. & Helenius, J. Quantification of surface tension and internal pressure generated by single mitotic cells. *Sci. Rep.* **4**, 6213 (2014).
30. Fouchard, J. et al. Curling of epithelial monolayers reveals coupling between active bending and tissue tension. *Proc. Natl. Acad. Sci. USA* **117**, 9377–9383 (2020).
31. Sui, L. et al. Differential lateral and basal tension drive folding of drosophila wing discs through two distinct mechanisms. *Nat. Commun.* **9**, 4620 (2018).
32. Fernández, P. A. et al. Surface-tension-induced budding drives alveologenesis in human mammary gland organoids. *Nat. Phys.* **17**, 1130–1136 (2021).
33. Guha Ray, C. & Haas, P. A. Unbuckling mechanics of epithelial monolayers under compression. *Phys. Rev. Lett.* **134**, 118402 (2025).
34. Andrenšek, U., Ziherl, P. & Krajnc, M. Wrinkling instability in unsupported epithelial sheets. *Phys. Rev. Lett.* **130**, 198401 (2023).
35. Rozman, J., Krajnc, M. & Ziherl, P. Morphologies of compressed active epithelial monolayers. *Eur. Phys. J. E* **44**, 99 (2021).
36. Luciano, M. et al. Cell monolayers sense curvature by exploiting active mechanics and nuclear mechanoadaptation. *Nat. Phys*. **17**, 1382–1390 (2021).
37. Harmand, N., Dervaux, J., Poulard, C. & Hénon, S. Thickness of epithelia on wavy substrates: measurements and continuous models. *Eur. Phys. J. E* **45**, 53 (2022).
38. Harmand, N., Huang, A. & Hénon, S. 3d shape of epithelial cells on curved substrates. *Phys. Rev. X* **11**, 031028 (2021).
39. Engstrom, T. A., Zhang, T., Lawton, A. K., Joyner, A. L. & Schwarz, J. M. Buckling without bending: A new paradigm in morphogenesis. *Phys. Rev. X* **8**, 041053 (2018).
40. Karzbrun, E., Kshirsagar, A., Cohen, S. R., Hanna, J. H. & Reiner, O. Human brain organoids on a chip reveal the physics of folding. *Nat. Phys.* **14**, 515–522 (2018).
41. Joyner, A. L., Willett, R. & Lawton, A.*Development of the Cerebellum from Molecular Aspects to Diseases* (Springer, 2017).
42. Krajnc, M. & Ziherl, P. cv Theory of epithelial elasticity. *Phys. Rev. E* **92**, 052713 (2015).
43. Štorgel, N., Krajnc, M., Mrak, P., Štrus, J. & Ziherl, P. Quantitative morphology of epithelial folds. *Biophys. J.* **110**, 269–277 (2016).
44. Haas, P. A. & Goldstein, R. E. Nonlinear and nonlocal elasticity in coarse-grained differential-tension models of epithelia. *Phys. Rev. E* **99**, 022411 (2019).
45. Wyatt, T. P. J. et al. Actomyosin controls planarity and folding of epithelia in response to compression. *Nat. Mater.* **19**, 109–117 (2020).
46. Moshe, M., Bowick, M. J. & Marchetti, M. C. Geometric frustration and solid-solid transitions in model 2d tissue. *Phys. Rev. Lett.* **120**, 268105 (2018).
47. Staddon, M. F., Hernandez, A., Bowick, M. J., Moshe, M. & Marchetti, M. C. The role of non-affine deformations in the elastic behavior of the cellular vertex model. *Soft Matter* **19**, 3080–3091 (2023).
48. Hernandez, A., Staddon, M. F., Bowick, M. J., Marchetti, M. C. & Moshe, M. Anomalous elasticity of a cellular tissue vertex model. *Phys. Rev. E* **105**, 064611 (2022).
49. Staple, D. B. et al. *Eur. Phys. J. E* **33**, 117–127 (2010).
50. Brau, F., Damman, P., Diamant, H. & Witten, T. A. Wrinkle to fold transition: influence of the substrate response. *Soft Matter* **9**, 8177–8186 (2013).
51. Razavi, M. J., Zhang, T., Liu, T. & Wang, X. Cortical folding pattern and its consistency induced by biological growth. *Sci. Rep.* **5**, 14477 (2015).
52. Holland, M., Budday, S., Goriely, A. & Kuhl, E. Symmetry breaking in wrinkling patterns: Gyri are universally thicker than sulci. *Phys. Rev. Lett.* **121**, 228002 (2018).
53. Alawiye, H., Kuhl, E. & Goriely, A. Revisiting the wrinkling of elastic bilayers i: linear analysis. *Philos. Trans. R. Soc. A* **377**, 20180076 (2019).
54. Alawiye, H., Farrell, P. E. & Goriely, A. Revisiting the wrinkling of elastic bilayers ii: Post-bifurcation analysis. *J. Mech. Phys. Solids* **143**, 104053 (2020).
55. Zavodnik, J., Košmrlj, A. & Brojan, M. Rate-dependent evolution of wrinkling films due to growth on semi-infinite planar viscoelastic substrates. *J. Mech. Phys. Solids* **173**, 105219 (2023).
56. Ebata, Y., Croll, A. B. & Crosby, A. J. Wrinkling and strain localizations in polymer thin films. *Soft Matter* **8**, 9086–9091 (2012).
57. Colin, J. & Holland, M. A. Layer wrinkling in an inhomogeneous matrix. *J. Mech. Mater. Struct.* **156-157**, 119–125 (2019).
58. Bal, P. K., Ouzeri, A. & Arroyo, M. Continuum theory for the mechanics of curved epithelial shells by coarse-graining an ensemble of active gel cellular surfaces. *J. Mech. Phys. Solids* **208**, 106477 (2026).
59. Kintses, B., van Vliet, L. D., Devenish, S. R. & Hollfelder, F. Microfluidic droplets: new integrated workflows for biological experiments. *Curr. Opin. Chem. Biol.* **14**, 548–555 (2010).
60. Kamiya, K., Kawano, R., Osaki, T., Akiyoshi, K. & Takeuchi, S. Cell-sized asymmetric lipid vesicles facilitate the investigation of asymmetric membranes. *Nat. Chem.* **8**, 881–889 (2016).
61. Bailles, A. et al. Genetic induction and mechanochemical propagation of a morphogenetic wave. *Nature* **572**, 467–473 (2019).
62. Hannezo, E. & Heisenberg, C.-P. Mechanochemical feedback loops in development and disease. *Cell* **178**, 12–25 (2019).
63. Bailles, A., Gehrels, E. W. & Lecuit, T. Mechanochemical principles of spatial and temporal patterns in cells and tissues. *Annu. Rev. Cell Dev. Biol.* **38**, 321–347 (2022).
64. Gelbart, M. A. et al. Volume conservation principle involved in cell lengthening and nucleus movement during tissue morphogenesis. *Proc. Natl. Acad. Sci. USA* **109**, 19298–19303 (2012).
65. Popkova, A. et al. A mechanical wave travels along a genetic guide to drive the formation of an epithelial furrow during drosophila gastrulation. *Dev. Cell* **59**, 400–414.e5 (2024).
66. Xie, K., Yang, Y. & Jiang, H. Controlling cellular volume via mechanical and physical properties of substrate. *Biophys. J.* **114**, 675–687 (2018).

67. Guo, M. et al. Cell volume change through water efflux impacts cell stiffness and stem cell fate. *Proc. Natl. Acad. Sci. USA* **114**, E8618–E8627 (2017).
68. Zehnder, S., Suaris, M., Bellaire, M. & Angelini, T. Cell volume fluctuations in mdck monolayers. *Biophys. J.* **108**, 247–250 (2015).
69. Venkova, L. et al. A mechano-osmotic feedback couples cell volume to the rate of cell deformation. *eLife* **11**, e72381 (2022).
70. Stoop, N., Lagrange, R., Terwagne, D., Reis, P. M. & Dunkel, J. Curvature-induced symmetry breaking determines elastic surface patterns. *Nat. Mater.* **14**, 337–342 (2015).

Acknowledgements

We thank Marko Popovic, Michael Moshe, and all the members of the Theoretical biophysics group at JSI for fruitful discussions. We thank Primož Ziherl and Tanmoy Sarkar for critically reading the manuscript. We acknowledge the financial support from the Slovenian Research and Innovation Agency (research projects J1-3009 and J1-60013, development funding pillar RSF-0106, and research core funding No. P1-0055). This research was also supported in part by grant no. NSF PHY-2309135 to the Kavli Institute for Theoretical Physics (KITP).

Author contributions

M.K. designed the research, U.A. performed the analytical calculations and numerical simulations. U.A. and M.K. wrote the manuscript.

Competing interests

The authors declare no competing interests.

Additional information

Supplementary information The online version contains supplementary material available at https://doi.org/10.1038/s42005-026-02547-1.

Correspondence and requests for materials should be addressed to Urška Andrenšek.

Peer review information *Communications Physics* thanks Yuehua Yang, Arthur Hernandez and the other, anonymous, reviewer(s) for their contribution to the peer review of this work.